



Quantum criticality of bandwidth-controlled Mott transition

Kensaku Takai *Department of Applied Physics, University of Tokyo, 7-3-1 Hongo, Bunkyo-ku, Tokyo 113-8656, Japan*Youhei Yamaji *Research Center for Materials Nanoarchitectonics (MANA) and Center for Green Research on Energy and Environmental Materials (GREEN), National Institute for Materials Science (NIMS), Namiki, Tsukuba-shi, Ibaraki 305-0044, Japan*

Fakher F. Assaad

*Institut für Theoretische Physik und Astrophysik and Würzburg-Dresden Cluster of Excellence ct.qmat, Universität Würzburg, Am Hubland, D-97074 Würzburg, Germany*Masatoshi Imada *Toyota Physical and Chemical Research Institute, 41-1 Yokomichi, Nagakute, Aichi 480-1192, Japan
and Research Institute for Science and Engineering, Waseda University, 3-4-1 Okubo, Shinjuku-ku, Tokyo 169-8555, Japan*

(Received 16 January 2023; revised 9 August 2023; accepted 10 August 2023; published 13 September 2023)

Metallic states near the Mott insulator show a variety of quantum phases, including various magnetic, charge-ordered states and high-temperature superconductivity in various transition metal oxides and organic solids. The emergence of a variety of phases and their competitions are likely intimately associated with quantum transitions between the electron-correlation-driven Mott insulator and metals characterized by its criticality, and is related to many central questions of condensed matter. The quantum criticality is, however, not well understood when the transition is controlled by the bandwidth through physical parameters such as pressure. Here, we quantitatively estimate the universality class of the transition characterized by a comprehensive set of critical exponents by using a variational Monte Carlo method implemented as an open-source innovated quantum many-body solver, with the help of established scaling laws at a typical bandwidth-controlled Mott transition. The criticality indicates a weaker charge and density instability in contrast to the filling-controlled transition realized by carrier doping, implying a weaker instability to superconductivity as well. The present comprehensive clarification opens up a number of routes for quantitative experimental studies for complete understanding of elusive quantum Mott transition and nearby strange metal that cultivate future design of functionality.

DOI: [10.1103/PhysRevResearch.5.033186](https://doi.org/10.1103/PhysRevResearch.5.033186)

I. INTRODUCTION

The Mott transition is a metal-insulator transition driven by the Coulomb repulsion of electrons in crystalline solids. It is driven either by controlling the ratio of the interaction strength to the bandwidth (bandwidth-controlled transition) or by carrier doping to the Mott insulator (filling-controlled transition) [1]. The two types of control are widely realized in organic solids [2,3] and transition metal compounds [1].

The filling-controlled transition has been relatively well studied motivated by the high-temperature superconductivity in the cuprates. Theoretically estimated criticality of the Mott transition was suggested to cause the charge instability that gives birth to severe competitions of the high-temperature superconductivity, strange metal, antiferromagnetism, ne-

maticity, and charge inhomogeneity including charge order in the cuprates [4–6]. It is also understood from the tendency toward the first-order transition that generates a miscibility gap in the carrier density near the Mott insulator. When the first-order transition can be suppressed, criticality emerges around the marginal quantum critical point (MQCP) [7]. The MQCP critical exponents have not been well explored in experiments, partly because various competing phases including superconductivity and effect of disorder preempt or mask criticality. However, the emergence of exotic phases including the superconductivity in the cuprates may be governed by the underlying MQCP and therefore the understanding of the MQCP has crucial importance to reveal the mechanism of the competing phases.

On the other hand, the bandwidth-controlled transitions have also been widely observed. They normally appear as first-order transitions, which terminate at a critical endpoint at nonzero temperatures. The universality class of this endpoint was proposed to belong to that of the classical Ising-model [8,9]. When the critical temperature is reduced to zero as the MQCP, the universality class should be distinct [7,10]. One of

Published by the American Physical Society under the terms of the Creative Commons Attribution 4.0 International license. Further distribution of this work must maintain attribution to the author(s) and the published article's title, journal citation, and DOI.

the central questions is whether the universality class can lead to strong quantum fluctuations and quantum entanglement, which triggers emergence of novel functionality including high-temperature superconductivity similarly to the incentive to gain insights for the filling-controlled case [6]. However, the bandwidth-controlled Mott transition at the MQCP and the related charge instability are not well explored even theoretically.

We summarize the basic structure around the MQCP of the metal insulator transition found in the earlier work, which is illustrated in Fig. 1 [10]. The MQCP appears as the endpoint of the finite-temperature critical line, namely, the endpoint of the first-order transition, while it also appears as the endpoint of the quantum critical line (QCL) running at temperature $T = 0$. The reason why the critical line continues beyond the MQCP is that the metal and insulator must always have a clear phase transition boundary at $T = 0$ unlike the case of the quantum Ising model such as that with the transverse magnetic field where the transition disappears beyond the conventional quantum critical point. Our focus in this paper is the universality class of the bandwidth-controlled MQCP and not the criticality of the QCL, because the MQCP is expected to show stronger quantum fluctuations and entanglement with enhanced charge fluctuations that may trigger exotic phases [10].

In the literature, the motivation of the study on the quantum critical point (QCP) in general has come from the expectations for novel physics, where finite critical temperature is lowered to zero and associated diverging quantum fluctuations emerge, which may induce exotic phases. In the present case, this corresponds to the MQCP appearing as a single point at $T = 0$, although the distinction between the MQCP and QCL is not well appreciated in the literature. The reason may be due to the fact that the QCL does not exist in the conventional critical point (QCP) arising from symmetry-breaking transitions. Along the quantum critical line (QCL), the criticality should be different from the MQCP in general.

Significance of the QCP including the MQCP is that the first-order transition starts from the QCP, which opens the possibility of coupling to divergent zero-wavenumber modes. In the case of the metal-insulator transition, this appears as the divergent charge fluctuations. However, the QCL exists even in the noninteracting case as in the simple band-insulator metal transition. For instance, in Ref. [10], the criticality of the MQCP was clarified for the filling-controlled transition in detail and the critical exponents are identified as $\alpha = -1$, $\beta = 1$, $\gamma = 1$, $\delta = 2$, $\nu = 1/2$ and $\eta = 0$, where $\gamma = 1$, and $\delta = 2$ lead to the divergence of the charge compressibility $\kappa \propto 1/x$, where x is the doping concentration. The divergent compressibility at the MQCP was supported in a 2D Hubbard model study [4]. In contrast, $\alpha = 0$, $\beta = 1$, $\gamma = 0$, $\delta = 1$, $\nu = 1/2$, and $\eta = 0$ were reported for the QCL. Here, the exponents $\alpha = 0$, $\gamma = 0$, and $\delta = 1$ imply that the fluctuations are not diverging. This is because of the absence of the opening of the first-order transition and indeed it is equivalent to the band-insulator-to-metal transition in usual noninteracting systems. The divergent charge fluctuations for the filling-controlled MQCP on the verge of the phase separation or the charge inhomogeneity opens the possibility of emergent exotic phases such as unconventional superconduc-

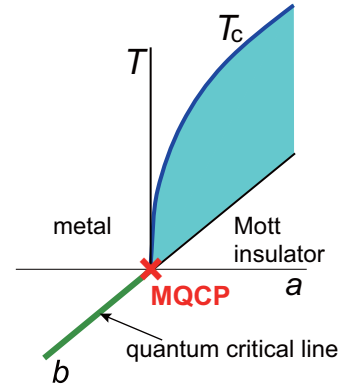


FIG. 1. Schematic phase diagram of Mott metal-insulator transition. The MQCP (red cross) is the quantum critical point between the metal and the Mott insulator and simultaneously the end point of the first order transition and the quantum critical line (green line). Finite-temperature critical point ($T = T_c$) (dark blue curve) appears as the endpoint of the first order boundary (light blue shaded surface). a and b represent the control parameters and are given by a combination of t_{\perp} and U in the present case. In the bandwidth-control case in general, the electron filling is fixed at an odd integer in this whole T - a - b parameter space. For details see Ref. [10].

tivity associated with this divergence and fluctuations. In the dynamical mean-field theory (DMFT) calculation, the metal-insulator critical point appears at a finite temperature, at which it was shown that the charge compressibility diverges [11]. However, in the DMFT, one cannot lower the critical temperature to zero to reach the MQCP, while in 2D one can see such an evolution to the MQCP. Therefore, it is natural to pose a question how the interplay between the diverging charge fluctuation and quantum fluctuations takes place at the MQCP for the bandwidth-controlled case in 2D. In other words, the nontriviality of the MQCP lies in the fact that the first-order metal-insulator transition and the resultant MQCP does not exist in the noninteracting case and it is purely the interaction effect. By considering this background and the significance with a direct connection to the quantum critical phenomena in general, we study the MQCP rather than the QCL. Then the universality of the QCL for the bandwidth-controlled transition is left for future studies.

In this article, we study the mechanism and criticality of the bandwidth-controlled quantum Mott transitions. For this purpose, we employ anisotropic two-dimensional Hubbard models at half filling as a typical example. We study the model by using a state-of-the-art variational Monte Carlo method (VMC) [12,13], where the open source code is available [14]. See Sec. VII A for details of the numerical method. The solution of the model shows the existence of the MQCP. We estimate a comprehensive set of critical exponents of the MQCP, which shows a perfect consistency with the scaling theory, which indicates a weaker charge and density instability in contrast to the filling-controlled transition by carrier doping, implying a weaker instability to superconductivity as well. Since the earlier experimental as well as theoretical studies by the dynamical mean-field study suggest the exponents different from the present results, we discuss the origin of the discrepancy.

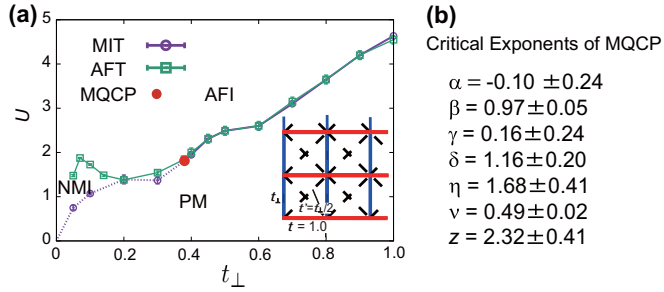


FIG. 2. (a) Ground-state phase diagram obtained by the present VMC calculation. The purple solid and broken lines with open circles indicate the first-order and continuous metal-insulator transition (MIT) boundaries, respectively. The green solid curve with open squares is for the antiferromagnetic transitions (AFT) (see Sec. VII D for the method to determine the MIT and see Appendix F for the AFT). Red large circle depicts the MQCP. Error bars are determined by considering the errors of size extrapolations and statistical errors of Monte Carlo calculations for finite-size systems. Inset: Lattice structure used for the present study; t - t_{\perp} - t' Hubbard model with the nearest-neighbor intrachain (red bonds), interchain (blue bonds), and next-nearest-neighbor (broken black bonds) hoppings t , t_{\perp} and $t' = t_{\perp}/2$, respectively. We take t as the energy unit. (b) Critical exponents of MQCP estimated in this article.

This paper is organized as follows: In Sec. II, we introduce the model. In Sec. III, the phase diagram is shown in the plane of the Hamiltonian parameters, which reveals the MQCP. In Sec. IV, the critical exponents of the MQCP are thoroughly estimated. In Sec. V, the estimated exponents are analyzed in terms of the scaling theory. Section VI is devoted to discussion and summary.

II. MODEL

For the purpose of clarifying the generic feature of the bandwidth-controlled Mott transition, as an example, we study the t - t_{\perp} - t' Hubbard model at half filling defined by the following Hamiltonian:

$$\hat{H} = -t \sum_{\langle i,j \rangle, \sigma} \hat{c}_{i\sigma}^{\dagger} \hat{c}_{j\sigma} - t_{\perp} \sum_{(i,j), \sigma} \hat{c}_{i\sigma}^{\dagger} \hat{c}_{j\sigma} + t' \sum_{\langle\langle i,j \rangle\rangle, \sigma} \hat{c}_{i\sigma}^{\dagger} \hat{c}_{j\sigma} + U \sum_i \hat{n}_{i\uparrow} \hat{n}_{i\downarrow}, \quad (1)$$

where $\hat{c}_{i\sigma}$ ($\hat{c}_{i\sigma}^{\dagger}$) annihilates (creates) a spin- σ electron at site i and $\hat{n}_{i\sigma}$ is its number operator. Here, t (t_{\perp}) is the hopping between the nearest-neighbor sites in the x (y) direction, t' is that between the next-nearest-neighbor sites and U represents the on-site Coulomb repulsion. The lattice structure of the present model is depicted in the inset of Fig. 2, where the intra-chain transfer t and interchain transfer t_{\perp} constituting the square lattice are geometrically frustrated with the next-nearest-neighbor transfer t' . The onsite Coulomb interaction U monitors the correlation effects and the control of U/t triggers the bandwidth-controlled Mott transition. In this model, by taking the nearest-neighbor transfer t along the chain direction as the energy unit, namely $t = 1$, the interchain hopping t_{\perp} acts as the parameter to control the dimensionality between 1D ($t_{\perp} = 0$) and 2D ($t_{\perp} = t$), which enables the control of the

Mott transition temperature to zero, namely allows us to study the MQCP. Here we fix the ratio of the next-nearest-neighbor hopping t' to t_{\perp} as $t' = t_{\perp}/2$.

Although we employ a specific model, the notion of universality that characterizes the 2D MQCP, renders the details of the model irrelevant. The MQCP essentially emerges between the metal and Mott insulator and it appears as the endpoint of both of the first-order transition and the continuous quantum critical line as sketched schematically in Fig. 1. In addition it does not retain the C_4 rotational symmetry, which is common to the experimental structure in the organic solids [2,3] and offer the possibility to capture the generic feature of the 2D MQCP. Although the transfer terms introduce slightly 1D-like anisotropy, we confirm that spin and charge fluctuations show isotropic singular behavior below and represents a typical 2D criticality. We obtain a comprehensive set of critical exponents that are consistent with each other in light of the scaling theory. In contrast to previous theoretical and experimental studies at finite temperatures $T > 0$ above the classical critical endpoint to infer a zero-temperature exponent [15,16], we focus on the quantum case directly at $T = 0$. We show, in Appendix A, the Fermi surface for the noninteracting case. It changes from 1D-like open Fermi surface for small t_{\perp} to 2D-like closed one by increasing t_{\perp} separated by the Lifshitz transition at $t_{\perp} \approx 0.62$. Similar models have been studied before [17–19]. Here we focus on the criticality of the Mott transition, for which we assume that the universality class does not depend on the details of the model.

III. PHASE DIAGRAM

We first summarize the obtained ground-state phase diagram of the metal, insulator and magnetic phases separated by metal-insulator and antiferromagnetic transitions in the parameter space of U and t_{\perp} in Fig. 2. Hereafter, we mainly focus on the metal-insulator transition. (Although we do not discuss details, the antiferromagnetic transition is discussed in Appendix F and I). For details of the method to determine the phase boundary, see Sec. VII C. The transition is of first-order for large t_{\perp} with a jump in physical quantities while it changes to a continuous one for smaller t_{\perp} detected only by the continuous opening/closing of the charge gap (see Appendix B). The first-order and continuous transitions meet at the MQCP. For the first-order part, the transition temperature as well as the 2D Ising nature of the transition vanishes at the MQCP. We find the MQCP roughly around $t_{\perp} = t_{\perp}^{\text{MQCP}} \sim 0.4$ and $U = U^{\text{MQCP}} \sim 1.8$, which will be more precisely estimated in the later part of this article. For $t_{\perp} > t_{\perp}^{\text{MQCP}}$, magnetic and metal-insulator transitions occur essentially simultaneously as a first-order transition. However, for $t_{\perp} < t_{\perp}^{\text{MQCP}}$, the two transitions become separated (see Appendix F for the magnetic transition) and a nonmagnetic insulator (NMI) phase emerges, but we do not go into details of the NMI and leave it for studies elsewhere. We also do not study the universality of the quantum critical line depicted as the purple dotted line in Fig. 2. Although the metal-insulator and antiferromagnetic transitions look slightly separated even for $0.2 < t_{\perp} < t_{\perp}^{\text{MQCP}}$, we do not exclude the possibility of a simultaneous transition within the numerical error bar. The overall phase structure obtained here is essentially similar to that obtained by the

cluster dynamical mean-field theory (CDMFT) at low temperature [20]. A small kinklike structure of the phase boundary around $t_{\perp} \sim 0.6$ is related to the Lifshitz transition in the corresponding noninteracting model (see Appendix A for the Fermi surface of the case $U = 0$).

IV. ESTIMATE OF MQCP AND ITS CRITICAL EXPONENTS

We now present our numerical results on the universality class at the MQCP. See Sec. VII C for definitions of the critical exponents, α , β , γ , δ , ν , z , and η analyzed below. Since we need to estimate the position of the MQCP first and the MQCP is defined by the point where the first-order transition disappears, we first estimate when the jump of physical quantities characteristic of the first-order transition vanishes. The conventional scaling analysis does not work accurately unless the MQCP point is precisely estimated.

The critical exponent β of the MQCP [Eq. (18)] is estimated from the jump of the double occupancy of electrons on the same site, $\Delta D = D_{\text{metal}} - D_{\text{ins}}$, where the double occupancy in the metallic (insulator) side is D_{metal} (D_{ins}) along the first-order transition line in the region $t_{\perp} > t_{\perp}^{\text{MQCP}}$ [see Eq. (12) for the definition of the double occupancy]. The fitting of the VMC numerical data in the range $0.4 \leq t_{\perp} \leq 0.9$ plotted in Fig. 3(a) shows that the mean squared error by defining the mean given by Eq. (18) becomes the minimum when we employ the MQCP point at $t_{\perp}^{\text{MQCP}} \sim 0.38 \pm 0.05$ and $\beta = 0.97 \pm 0.05$ as is shown in Secs. VII C and VII D [Fig. 5(a)]. The green curve in Fig. 3(a) is the resultant optimized fitting. The error bar for $t_{\perp}^{\text{MQCP}} = 0.38$ estimated by the bootstrap method (see Sec. VII D for details of the bootstrap) is included in the error bar of β . The estimated β is similar to $\beta = 1$ in the filling-controlled transition predicted in the literature [7].

We also simultaneously determine the critical value of U at the MQCP and critical exponents δ and νz by the combined analysis with Eq. (29) at $t_{\perp}^{\text{MQCP}} = 0.38$, and obtain $U^{\text{MQCP}} = 1.83 \pm 0.03$, $\nu z = 1.13 \pm 0.19$, $\delta_I = 0.98 \pm 0.03$, and $\delta_M = 1.05 \pm 0.04$ (see Figs. 3(b) and 4 as well as Secs. VII C and VII D), where δ is estimated separately in the insulating (δ_I) and in the metallic (δ_M) phases.

These results imply that the nonsingular linear term proportional to $|U - U^{\text{MQCP}}|$ makes the precise estimate of δ difficult, if $\delta \leq 1$. However, we will clarify that $\delta \sim 1.0$ is consistent with other scaling analyses. The exponent is the same again with the filling-controlled MQCP estimated as $\delta = 1$ in Refs. [7,10] within the statistical error.

V. SCALING ANALYSIS

In our calculation, we obtained $\beta \sim 1.0$, $\nu z \sim 1.1$, and $\delta \sim 1.0$. We now analyze this result in the framework of scaling theory. Here, the singular part of the ground-state energy E around the MQCP satisfies the form

$$E \propto \xi^{-(d+z)}, \quad (2)$$

where ξ is the unique length scale that diverges at the MQCP, and d and z are the spatial dimension and the dynamical exponent, respectively. This scaling theory was examined in

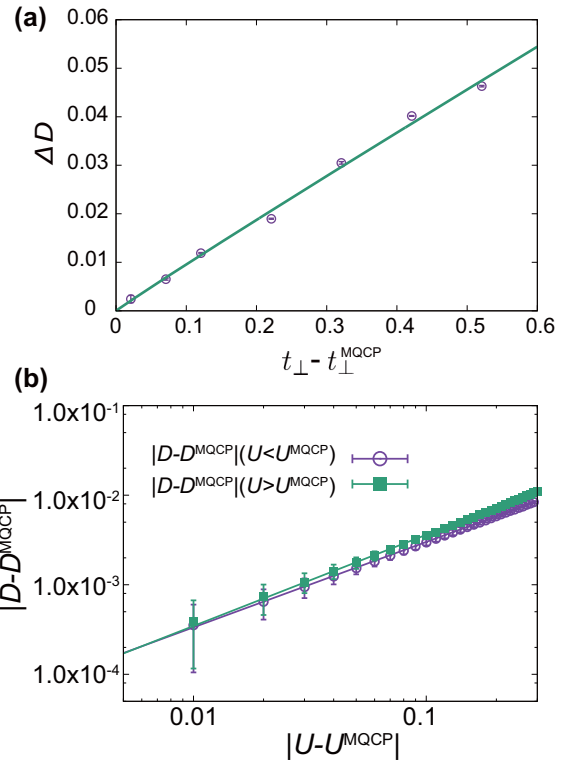


FIG. 3. (a) t_{\perp} -dependence of jumps of extrapolated double occupancy ΔD with the choice of $t_{\perp}^{\text{MQCP}} = 0.38$ determined in Sec. VII C. Green curve represents the optimized fitting leading to $\beta = 0.97 \pm 0.05$. (b) U dependence of extrapolated double occupancy D at $t_{\perp}^{\text{MQCP}} = 0.38$. Green (purple) line represents the fittings to estimate δ_I for $U > U^{\text{MQCP}}$ (δ_M for $U < U^{\text{MQCP}}$), which indicate $\delta_I = 0.98 \pm 0.03$ and $\delta_M = 1.05 \pm 0.04$.

Ref. [10], where critical exponents satisfy the following scaling relations:

$$\gamma = \beta(\delta - 1), \quad (3)$$

$$2 - \eta = \gamma/\nu \quad (\text{Fisher's relation}), \quad (4)$$

$$\alpha + 2\beta + \gamma = 2 \quad (\text{Rushbrooke's relation}), \quad (5)$$

$$2 - \alpha = (d + z)\nu \quad (\text{Josephson's relation}). \quad (6)$$

All the scaling laws here can be derived from Eq. (2).

Since the metal is characterized by a nonzero carrier density X as the natural order parameter in distinction from the insulator ($X = 0$), the unique length scale ξ that diverges at the MQCP must be the mean carrier distance given by

$$\xi \propto X^{1/d}. \quad (7)$$

In this case, we obtain

$$\delta = z/d. \quad (8)$$

The relation holds for both the bandwidth- and filling-control transitions. In the bandwidth-control case, X in the metallic phase is the density of unbound doublon (double occupancy site) and holon (electron empty site). The last available scaling

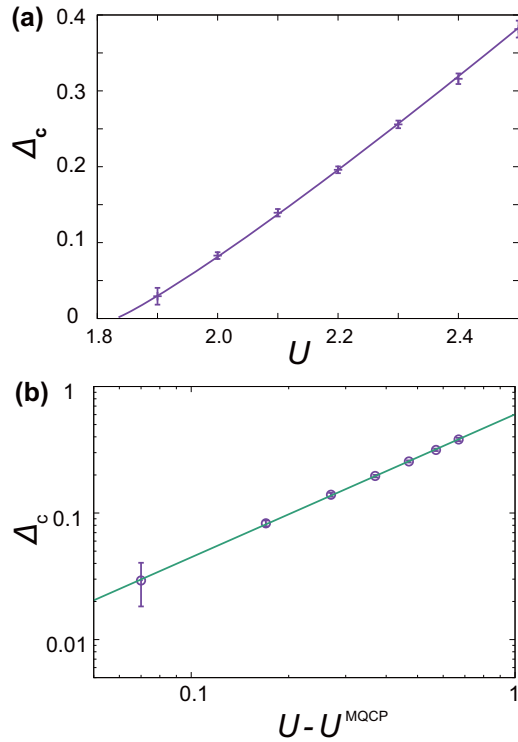


FIG. 4. The exponent νz estimated from the charge gap Δ_c at MQCP. U dependence of Δ_c in the linear plot (a) and the logarithmic scaling plot (b) for 28×28 site around the MQCP ($t_{\perp}^{\text{MQCP}} = 0.38$ and $U^{\text{MQCP}} = 1.83$). Purple curve in panel (a) and green line in panel (b) show the same fitting by the estimate of the MQCP point and the critical exponents, indicating $\nu z = 1.13 \pm 0.19$.

relation is

$$\nu = \beta/d. \quad (9)$$

See Ref. [10] and Methods C for the derivation of the scaling laws.

By using these relations, if only $\beta = q$ and $\nu z = p$ are known, other exponents can be obtained for $d = 2$ as $\alpha = 2 - (p + q)$, $\gamma = p - q$, $\delta = p/q$, $\eta = 4 - 2p/q$, $\nu = q/2$, and $z = 2p/q$. By using the values $p \sim 1.13 \pm 0.19$ and $q \sim 0.97 \pm 0.05$ obtained by our simulation, we find the exponents listed in Fig. 2(b), which can be consistent with $\alpha \sim 0$, $\gamma \sim 0$, $\delta \sim 1.0$, $\eta \sim 2.0$, $\nu \sim 1/2$, and $z \sim 2$. In fact, our numerical result obtained independently from the scaling of $D - D_c$ indicates $\delta \sim 1$, which is consistent with this prediction. Furthermore, the spatial correlation of the double occupancy D can be used to estimate $z + \eta$ independently from the above estimates, and though the estimate contains a large error bar, it suggests $z + \eta \sim 3.3 \pm 0.8$ (see Sec. VII C and Appendix G), which is again consistent with 4.0 estimated from the scaling theory.

VI. DISCUSSION AND SUMMARY

The quantum critical exponent $\nu z \sim 0.6 \sim 0.9$ was indirectly estimated above the classical Ising-type critical temperature of the first-order Mott transition, aiming at es-

timating the quantum criticality by calculating the resistivity along the Widom line continued above the critical temperature by using the DMFT [15,21]. It was compared with experimental measurements of organic solids, semiconductor moiré superlattices and transition metal dichalcogenides, because they all infer the $T = 0$ criticality again from the Widom line [16,22,23]. They also argued that the exponent does not appreciably change with the character of the neighboring phases [16] implying a universal and robust criticality. Ambiguities of the definition of the Widom line and the estimate at temperature above nonzero critical temperature, however, have yielded a variety of estimates for the exponent. By taking into account this ambiguity and also possible errors often recognized in the exponents estimated from the collapse to a single scaling plot employed by them (see also the next paragraph), and by considering a considerable variation of their estimates do not necessarily contradict our estimate of $\nu z \sim 1.13 \pm 0.19$.

More importantly, the estimate by the DMFT [15,21] is rigorous at infinite dimensions and the exponents can be different from the present two-dimensional case. Another DMFT study [24] suggested that the estimated νz in Ref. [15] is related to the exponent of the instability line of the metastable insulating state at the boundary of the coexisting region. This instability line should vanish if the finite-temperature critical temperature is lowered to zero as in the MQCP. Therefore in this regard as well, νz estimated along the Widom line may not necessarily have a connection to the MQCP exponent studied here. If one wishes to estimate the MQCP exponents focused in this article, then it is desired to estimate the exponent by sufficiently suppressing the critical temperature both in the theoretical and experimental studies. Our analysis has determined a more comprehensive and quantitative set of various exponents β , δ , νz and $z + \eta$ from the scaling of four independent quantities including the double occupancy and charge gap, by straightforward estimates directly at zero temperature precisely for the MQCP. The four exponents are shown to satisfy a perfect consistency with the scaling theory and determine all the exponents.

Though we obtained $d + z \sim 4$ as if it were at the upper critical dimension of the conventional symmetry-breaking magnetic transition, it does not necessarily mean that the simple mean-field treatment is justified, because the Mott transition is not primarily a symmetry-breaking transition. Indeed, the anomalous dimension drives the nonzero and a fairly large exponent for η (~ 2), which can be analyzed as a Lifshitz-type topological transition that makes vanishing Fermi-surface pocket [25]. In fact, the exponents $\gamma \sim 0$, $z \sim 2$ and $\delta \sim 1$ look similar to a case of the 2D Lifshitz transition described by the emergence of electron and hole pockets [25].

The exponents $\alpha = \gamma \sim 0$ and $\delta \sim 1$ indicate that the bandwidth-controlled MQCP does not drive divergent fluctuations in the charge channel, because the susceptibilities (the second derivatives of the energy with respect to t_{\perp} and U) are not divergent at the MQCP. This is also indicated by nonsingular dependence of the energy as a function of the electron density at the MQCP as is shown in Fig. 10 in the Appendix. This absence is in contrast with the filling-controlled MQCP, where the divergent charge fluctuations and the charge inhomogeneity are obtained as a common property

[4,26,27]. The charge instability is also tightly linked with a strong effective attraction of the carriers [5,10], which may be absent here. This is obviously a disadvantageous aspect for the promotion for the superconductivity. Since the present simple model and its MQCP do not have any special aspect or unique symmetry, the universality class found here may be a standard one applicable widely to 2D MQCP.

On the other hand, the antiferromagnetic transition does not contradict mean-field-like normal divergent fluctuation with divergent susceptibility as is clarified in Appendix F. The antiferromagnetic transition seems to occur at slightly larger U ($U^{\text{AF}} \sim 1.85$) than $U^{\text{MQCP}} \sim 1.83$, but it is not easy to pin down whether they really differ (see Appendix F). Nevertheless, the estimated $\nu^{\text{AF}} \sim 0.5$ and $\eta^{\text{AF}} + z^{\text{AF}} \sim 2$ definitely indicate divergent fluctuations characterized by $\gamma^{\text{AF}} > 0$ and $\delta^{\text{AF}} > 1$ with the help of the scaling law independently of the Mott criticality. In any case, in the scaling properties, metal-insulator transition at the MQCP and the antiferromagnetic transition are decoupled as we show in Appendix I. Therefore, the universality and critical exponents of the MQCP are not affected by either antiferromagnetic or paramagnetic nature of the insulating phase and the present system is expected to represent the general and universal bandwidth-controlled 2D Mott transition.

We also note that the spin and charge correlations show essentially 2D isotropic correlations as we see in Figs. 14 and 15 and manifests the 2D nature at the MQCP.

We summarize the significance of the present paper:

(1) The comprehensive set of critical exponents β , γ , δ , η , ν , and z , is estimated with consistency with the scaling theory. Our estimate provides us with a unified understanding of the universality class of clean $D = 2$ MQCP for the bandwidth-controlled Mott transition. This is the same situation that the experiments in the literature aimed at.

(2) The exponents are estimated directly at $T = 0$ unlike most of the previous studies.

(3) The employed numerical method is a state-of-the-art quantum many-body solver provided as the open-source software mVMC, which can treat spatial and temporal quantum fluctuations.

(4) The present comprehensive clarification opens up a number of possible routes to test by experimental studies for complete understanding of quantum Mott transition and nearby strange metal, which is expected to serve for future design of functionality.

VII. METHODS

A. Numerical method

For the ground-state calculations, we employ a variational Monte Carlo (VMC) method [12,13]. The optimization procedure of the VMC method to reach the ground state is equivalent to the imaginary time (τ) evolution represented by the repeated operation of $\exp(-\tau H)$ for the Hamiltonian H or equivalently natural gradient method [28,29]. We choose the periodic-antiperiodic boundary condition, i.e., $x(y)$ direction is periodic (antiperiodic) because its boundary condition allows closed shell condition for $L \times L = 4n \times 4n$ lattices,

which makes the optimization of the variational parameters easier and statistical errors smaller due to the reduced degeneracy. It also makes the extrapolation to the thermodynamic limit easier in the later procedure. We use the trial wave function with correlation factors and the spin quantum-number projection as

$$|\psi\rangle = \mathcal{L}^S \mathcal{P}_G \mathcal{P}_J \mathcal{P}_{\text{dh}}^{(4)} |\phi_{\text{pair}}\rangle, \quad (10)$$

where \mathcal{P}_G , \mathcal{P}_J , $\mathcal{P}_{\text{dh}}^{(4)}$ are Gutzwiller, Jastrow, and doublon-holon correlation factors and \mathcal{L}^S is the spin quantum-number projection. First, we give the pair-product wave function, defined as

$$|\phi_{\text{pair}}\rangle = \left(\sum_{i,j=1}^{N_s} f_{ij} \hat{c}_{i\uparrow}^\dagger \hat{c}_{j\downarrow}^\dagger \right)^{N_e/2} |0\rangle, \quad (11)$$

where N_s is the number of sites and N_e is the number of electrons. This wave function has the same form as the Bardeen-Cooper-Schrieffer (BCS) wave function, in which the spins are always restricted to pairs of up and down spins representing the singlet. The pair product function can also represent any form of the Slater determinant and in addition it has representability of any mean-field solution including magnetic, charge and superconducting symmetry breaking.

The averaged double occupancy

$$D = \sum_i \langle \hat{n}_{i\uparrow} \hat{n}_{i\downarrow} \rangle / N_s, \quad (12)$$

where $\hat{n}_{i\uparrow}$ ($\hat{n}_{i\downarrow}$) is the number operator of spin-up (spin-down) electrons, is a key quantity to understand strong correlation effects, especially in the Hubbard model, where $\langle \dots \rangle = \langle \psi | \dots | \psi \rangle / \langle \psi | \psi \rangle$ is the expectation value in the ground state. In fact, the double occupancy is controlled by the Gutzwiller factor [30]

$$\mathcal{P}_G = \exp \left(-g \sum_i \hat{n}_{i\uparrow} \hat{n}_{i\downarrow} \right) \quad (13)$$

to lower the energy where g is a variational parameter.

To take into account the long-ranged charge correlation, we also introduce the Jastrow factor [31]

$$\mathcal{P}_J = \exp \left(-\frac{1}{2} \sum_{i \neq j} v_{ij} \hat{n}_i \hat{n}_j \right), \quad (14)$$

where v_{ij} are variational parameters and $\hat{n}_i \equiv \hat{n}_{i\uparrow} + \hat{n}_{i\downarrow}$ is the number operator of electrons.

To express the correlation between doublon (site doubly occupied by the spin-up and spin-down electrons) and holon (empty site) in the strongly correlated regions, we introduce a four-site doublon-holon correlation factor

$$\mathcal{P}_{\text{dh}}^{(4)} = \exp \left(-\sum_{m=0}^4 \sum_{i=1}^{N_s} (\alpha_m^{\text{d}} \xi_{im}^{\text{d}} + \alpha_m^{\text{h}} \xi_{im}^{\text{h}}) \right), \quad (15)$$

where $\xi_{im}^{\text{d(h)}}$ denotes the number operator of doublon (holon) around i th site. and $\alpha_m^{\text{d(h)}}$ are the variational parameters. We can express the operator $\xi_{im}^{\text{d(h)}}$, for example, as $\xi_{i4}^{\text{d}} \equiv$

$\hat{D}_i \prod_{\ell} \hat{H}_{i+\ell}$ and $\xi_{i0}^h \equiv \hat{H}_i \prod_{\tau} (1 - \hat{D}_{i+\tau})$, where $i + \ell$ and $i + \tau$ run the nearest-neighbor sites around i and \hat{D}_i (\hat{H}_i) is the doublon (holon) operator defined as $\hat{D}_i = \hat{n}_{i\uparrow} \hat{n}_{i\downarrow}$ [$\hat{H}_i = (1 - \hat{n}_{i\uparrow})(1 - \hat{n}_{i\downarrow})$].

All of the parameters f_{ij} , g , v_{ij} , α_m^d , α_m^h defined in Eqs. (11), (13)–(15) are variational parameters and they are optimized to lower the energy simultaneously by following the standard natural gradient method (stochastic reconfiguration method) [28]. We set the 2×2 -sublattice structure for the pairing wave function $|\phi_{\text{pair}}\rangle$ to reduce the variational parameters.

We calculate several physical quantities to identify the ground state. To determine the magnetic order and to distinguish a metal from an insulator, we calculate relevant physical quantities, i.e., the momentum distribution function $n(\vec{k})$ and the spin structure factor $S(\vec{q})$.

Momentum distribution function $n(\vec{k})$ is given by

$$n(\vec{k}) = \frac{1}{2N_s} \sum_{i,j,\sigma} \langle \hat{c}_{i\sigma}^\dagger \hat{c}_{j\sigma} \rangle e^{i\vec{k} \cdot (\vec{r}_i - \vec{r}_j)}, \quad (16)$$

where \vec{r}_i is the vector representing the coordinate of i th state.

In the same way, the spin structure factor $S(\vec{q})$ is calculated from

$$S(\vec{q}) = \frac{1}{3N_s} \sum_{i,j} \langle \hat{S}_i \cdot \hat{S}_j \rangle e^{i\vec{q} \cdot (\vec{r}_i - \vec{r}_j)}. \quad (17)$$

In the VMC calculations, we prepared several different initial states [such as the paramagnetic metal (PM) (free fermion) and antiferromagnetic insulator (AFI) states] and optimized them until the variational parameters reach the convergence, which may not necessarily preserve the character of the initial states and the nature of the optimized state is identified only after calculating physical quantities. To investigate the metal-insulator and magnetic transitions in the thermodynamic limit, we perform calculations of energy and other physical quantities on the $L \times L$ site square lattice with the periodic-antiperiodic boundary condition for $L = 16, 20, 24$, and 28 for each initial state and the size dependences are examined.

In this article, we perform the size extrapolations and scaling analyses to examine the magnetic order and metallicity in the thermodynamic limit.

This basic method is widely used and was tested from various perspectives in a number of benchmarks [13,32,33]. Of course, it can represent various mean-field wave functions such as charge, spin-ordered, and superconducting states as well as fermi liquid metals. It was also shown that the strongly correlated fermionic states such as Tomonaga-Luttinger liquid and quantum spin liquid are well captured by the present wave function. The applicability ranges from 2D itinerant Hubbard model to frustrated quantum spin models, which has proven to show one of the best accuracies among available quantum many-body solvers for strongly correlated quantum lattice systems. Readers are referred to Refs. [4,14,33,34]. Note that the conventional auxiliary-field quantum Monte Carlo method has severe sign problem in geometrically frustrated systems even at half filling. We confirmed that the present case exhibits desperate sign difficulty of AFQMC at and near the MQCP for systems beyond the size 12×12 , which are, however

necessary to analyze the nature of MQCP. See the average sign plotted in Fig. 18 in Appendix J. In the present case, the ground state energy per site E/N obtained from precisely the same VMC method using the form of the wave function Eq. (10) and the same Hamiltonian at the MQCP, $t_\perp = 0.38$ and $U = 1.83$ for 4×4 lattice with the periodic-antiperiodic boundary condition is -0.8665 ± 0.0005 , while the value obtained from the exact diagonalization is -0.8700 . The error $\sim 0.4\%$ is similar to the case of the benchmark in Ref. [13]. See also Appendix J. For physical quantities, the double occupancy $D = 0.1869 \pm 0.0003$ and the peak of the spin structure factor $S(\vec{q}) = 0.4489 \pm 0.0008$ at (π, π) are compared with the exact values 0.1844 and 0.4301 , respectively. This benchmark and that in the literature show that the accuracy well withstands and can be used for the present analyses. See also Appendix J.

B. Definition of critical exponents and derivation of scaling laws

Here, the double occupancy D is regarded as a natural order parameter of the metal-insulator transition. We calculate the critical exponents for the extrapolated double occupancy D by controlling t_\perp and U , where the scheme for the extrapolation is given in Appendix G. The exponent β is defined from the asymptotic scaling form between the jumps of D (namely, ΔD) and t_\perp measured from the critical point, i.e.,

$$\Delta D(t_\perp) = a |t_\perp - t_\perp^{\text{MQCP}}|^\beta \quad (18)$$

near the MQCP point t_\perp^{MQCP} , where a is a constant.

The critical exponents δ and γ are defined from

$$D - D^{\text{MQCP}}|_{t_\perp=t_\perp^{\text{MQCP}}} \propto |U - U^{\text{MQCP}}|^{1/\delta}, \quad (19)$$

$$\left. \frac{dD}{dU} \right|_{U=U_c} \propto |t_\perp - t_\perp^{\text{MQCP}}|^{-\gamma}. \quad (20)$$

The definition of the exponent α is given from

$$\frac{d^2 E}{dt_\perp^2} \propto |t_\perp - t_\perp^{\text{MQCP}}|^{-\alpha} \quad (21)$$

for the ground-state energy E .

Insulators are distinguished from metals by a nonzero charge gap Δ_c , which is numerically defined by

$$\Delta_c \equiv \frac{1}{2} [\mu(N_\uparrow + N_\downarrow + 1) - \mu(N_\uparrow + N_\downarrow)], \quad (22)$$

where the chemical potential μ is given as $\mu(N_\uparrow + N_\downarrow + 1) = [E(N_\uparrow + 1, N_\downarrow + 1) - E(N_\uparrow, N_\downarrow)]/2$, and $E(N_\uparrow, N_\downarrow)$ is the optimized ground-state energy for systems with the number of spin-up (spin-down) electrons N_\uparrow (N_\downarrow). The scaling of the charge gap around the MQCP at $U = U^{\text{MQCP}}$ is defined as

$$\Delta_c(U) = a_U |U - U^{\text{MQCP}}|^{\nu z}, \quad (23)$$

where ν is the correlation-length exponent and z is the dynamical exponent. Here, a_U is a constant. This relation is the consequence of the scaling of the energy scale [15,16], $\Delta_c \propto \xi^{-z}$, where ξ is the unique length scale which diverges at the MQCP. The dynamical exponent relates the length (momentum) to time (energy) scale and the correlation-length exponent ν is defined from

$$\xi \propto |t_\perp - t_\perp^{\text{MQCP}}|^{-\nu}. \quad (24)$$

Scaling relations Eqs. (8) and (9) are derived in the following way [10]: The scaling of the energy, Eq. (2) is rewritten as $E \propto X^{(d+z)/d}$ by using Eq. (7). By adding the t_{\perp} and U dependences, E has the form

$$E = -UX + B_0(t_{\perp} - t_{\perp}^{\text{MQCP}})X^{\phi} + CX^{(d+z)/d}. \quad (25)$$

Minimizing E for $t_{\perp} - t_{\perp}^{\text{MQCP}} = 0$ gives the scaling between X and $U - U^{\text{MQCP}}$, namely δ leading to Eq. (8). Equations (8), (18), and (24) lead to Eq. (9).

The correlation of double occupancy is determined by

$$Q(\vec{r}) = \frac{1}{N_s} \sum_{\vec{r}'} \langle (\hat{D}(\vec{r} + \vec{r}') - \langle \hat{D} \rangle)(\hat{D}(\vec{r}') - \langle \hat{D} \rangle) \rangle, \quad (26)$$

where $\hat{D}(\vec{r}) = \hat{n}_{\vec{r}\uparrow}\hat{n}_{\vec{r}\downarrow}$ is the double occupancy operator and $\langle \hat{D} \rangle$ is the spatially averaged expectation value in the ground state. In the scaling hypothesis, this correlation is expected to follow

$$Q(\vec{r}) \propto r^{-(d+z+\eta-2)} \quad (27)$$

at asymptotically long distance $r = |\vec{r}|$.

C. Methods for determination of metal-insulator transition and MQCP

In the region of first-order transitions, we see the energy level crossing between PM and AFI states, which accompanies a jump of the double occupancy ΔD . The first-order transition point is identified by this energy level crossing after the system size extrapolation to the thermodynamic limit. The metal-insulator transition is corroborated by the opening of the charge gap and the qualitative change of the momentum distribution in Appendix D, Fig. 9 depicted for $t_{\perp} = 0.5, 0.7$, and 1.0. In most of the first-order region, we have confirmed that the transition indeed represents the simultaneous transition of metal-insulator and antiferromagnetic transitions by examining several relevant physical quantities around the transition point. We have determined the continuous metal-insulator transition by the opening of the charge gap as is described in Fig. 7 in Appendix C

The MQCP point is first determined from the point where ΔD vanishes as is plotted in Fig. 3(a). To determine t_{\perp}^{MQCP} and β simultaneously, we have performed a regression analysis to optimize t_{\perp} and β dependencies of ΔD in the form Eq. (18) by minimizing the following χ^2 :

$$\chi^2 = \sum_i^{N_{\text{sample}}} (\Delta D_i - \Delta D_{\text{fit}})^2 / (N_{\text{sample}} - 2) \quad (28)$$

for N_{sample} data point, where ΔD_{fit} has the form (18) and ΔD_i is the simulation data. The logarithmic difference is appropriate to estimate the error for the power-law function. In Fig. 5(b), t_{\perp} dependence of χ^2 is plotted for the optimized exponent β . From the minimum of χ^2 , t_{\perp}^{MQCP} is determined as 0.38 ± 0.05 , where β is 0.97 ± 0.05 . The error bar is estimated from the bootstrap analysis explained in Sec. VII D.

Since the MQCP can be signaled by the criticality given by the exponents β , δ , νz , and the opening of the charge gap, the value of U^{MQCP} is estimated by the combined analysis of these three by employing $t_{\perp}^{\text{MQCP}} = 0.38$ as is analyzed in Fig. 5(a),

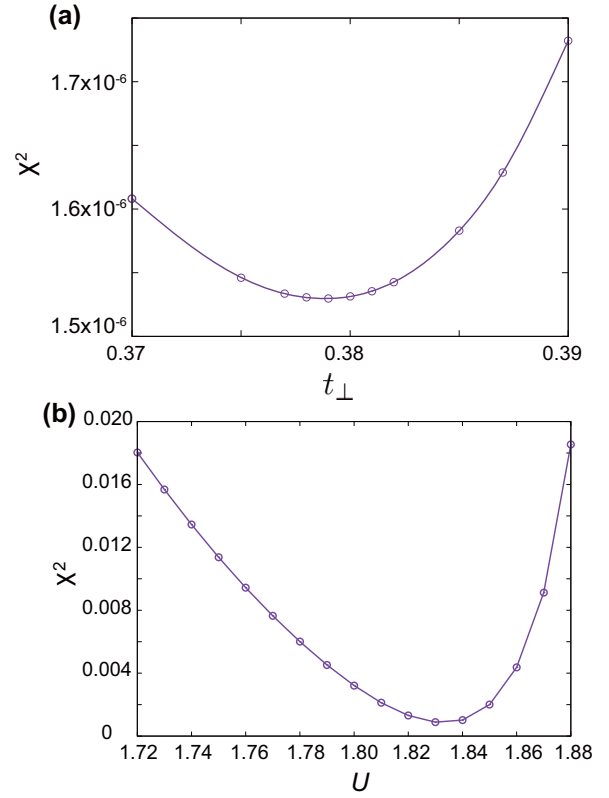


FIG. 5. (a) t_{\perp} -dependence of χ^2 value for the fitting Eq. (18), which results in $t_{\perp}^{\text{MQCP}} = 0.38 \pm 0.05$ and $\beta = 0.97 \pm 0.05$. (b) U dependence of χ^2 value for the fittings to combined Eq. (19) and Eq. (23), which results in $U^{\text{MQCP}} = 1.83 \pm 0.03$, $\nu z = 1.13 \pm 0.19$, $\delta_I = 0.98 \pm 0.03$, and $\delta_M = 1.05 \pm 0.04$.

where the minimum of the χ^2 value now defined as

$$\begin{aligned} \chi^2 = & \sum_i^{N_{U\text{-sample}}} (\ln \Delta_{ci} - \ln \Delta_{c\text{fit}})^2 / (N_{U\text{-sample}} - 2) \\ & + \sum_i^{N_{U1\text{-sample}}} (\ln |D_{Ii} - D^{\text{MQCP}}| - \ln |D_{\text{fit}} - D^{\text{MQCP}}|)^2 / \\ & (N_{U1\text{-sample}} - 2) \\ & + \sum_i^{N_{UM\text{-sample}}} (\ln |D_{Mi} - D^{\text{MQCP}}| - \ln |D_{\text{fit}} - D^{\text{MQCP}}|)^2 / \\ & (N_{UM\text{-sample}} - 2) \end{aligned} \quad (29)$$

suggests $U^{\text{MQCP}} = 1.83 \pm 0.03$, $\nu z = 1.13 \pm 0.19$, $\delta_I = 0.98 \pm 0.03$, and $\delta_M = 1.05 \pm 0.04$. For fittings to obtain these critical exponents, we assume Eqs. (19) and (23).

D. Interpolation and bootstrap techniques

To estimate metal-insulator transition points, we introduce the interpolation techniques by fitting the computed data to

an assumed form. For reliable estimates for metal-insulator transition points, we interpolate energy and double occupancy data as a function of U by the cubic function as

$$f(U) = a_0 U^3 + a_1 U^2 + a_2 U + a_3 \quad (30)$$

as the best fit of the U dependence of quantities. The crossing point of the interpolated energy of each metallic and insulating state gives us a reliable estimate of the level crossing point for the first-order transition.

In addition, we estimate the error bar of the level crossing point by using the bootstrap method. Ground-state energy estimated by our Monte Carlo calculation, E_{MC} contains statistical errors given by the standard deviation σ_{MC} . Namely, we assume that E_{MC} obeys the Gaussian distribution $P(E_{MC}, \sigma_{MC}^2)$ and perform the following procedure:

(1) Generate a number of synthetic samples of the energy which follows the probability $P(E_{MC}, \sigma_{MC}^2)$ around the interpolated U dependence of the energy given by Eq. (30) for both insulating and metallic states.

(2) Calculate the crossing point between the insulating and metallic states for each synthetic data.

(3) Calculate the variance of the crossing points of the synthetic data, which gives the estimate of the error bar.

Furthermore, we also apply the bootstrap method for determining statistical errors for critical exponents and t_{\perp}^{MQCP} and U^{MQCP} in Sec. VII D.

ACKNOWLEDGMENTS

The authors acknowledge Macin Raczowski for useful discussions. M.I. acknowledges the support of MEXT KAKENHI, Grant-in-Aid for Transformative Research Areas, Grants No. JP22H05111 and No. JP22H05114 and JSPS KAKENHI Grants No. JP16H06345 and No. JP19H00658. This research was also supported by MEXT as “program for Promoting Researches on the Supercomputer Fugaku” (Basic Science for Emergence and Functionality in Quantum Matter—Innovative Strongly Correlated Electron Science by Integration of Fugaku and Frontier Experiments, Grants No. JPMXP1020200104 and No. JPMXP1020230411). We thank the Supercomputer Center, the Institute for Solid State Physics, University of Tokyo for the use of the facilities. We also thank the computational resources of supercomputer Fugaku provided by the RIKEN Center for Computational Science (Project IDs No. hp210163 and No. hp220166) and Oakbridge-CX in the Information Technology Center, The University of Tokyo. F.F.A. thanks the DFG for funding via the Wurzburg-Dresden Cluster of Excellence on Complexity and Topology in Quantum Matter ct.qmat (EXC 2147, Project ID No. 390858490).

APPENDIX A: SHAPE OF FERMI SURFACE FOR NONINTERACTING SYSTEM

Figure 6 shows the Fermi surface for $U = 0$.

APPENDIX B: CHARGE GAPS IN CONTINUOUS TRANSITION REGION

Charge gap defined by Eq. (23) is obtained from the procedure in Sec. VII C. An example of the calculated results

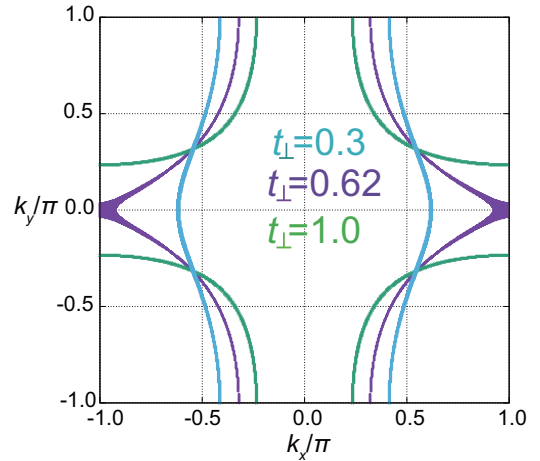


FIG. 6. Fermi surfaces of the model for $U = 0$ at half filling. Green, purple, and light-blue curves indicate the Fermi surface at $t_{\perp} = 1, 0.62$, and 0.3 , respectively.

for 28×28 lattices in the cases of (a) $t_{\perp} = 0.05$, (b) 0.1 , (c) 0.2 , and (d) 0.3 are shown in Fig. 7. The phase boundary of metal-insulator transitions in Fig. 1 is determined by analyzing these results. The size of the artifact by the finite-size gap Δ_0 speculated from the noninteracting case is illustrated by the horizontal dotted line.

APPENDIX C: METHOD TO ESTIMATE THE CHARGE GAP IN PHASE SEPARATION REGION

Figure 8(a) shows that the energy as functions of n shows phase separation for $U \geq 1.9$ in case of $t_{\perp} = 0.38$. The carrier density n is defined as $n = N_e/N_s - 1/2$. Figure 8(b) illustrates the procedure to estimate the charge gap when the phase separation takes place. Convex (concave) downward curve of the chemical potential in the electron (hole) doped region indicate the phase separation. By drawing the horizontal line to make the area of the two regions surrounded by the horizontal line and the chemical potential curve, the phase separation region can be obtained, where the pinned chemical potential during the phase separation is given by the horizontal line. The difference in the pinned chemical potential between the hole and electron doped sides is the charge gap.

APPENDIX D: MOMENTUM DISTRIBUTION FUNCTIONS IN FIRST-ORDER TRANSITION REGION

In most of the first-order transition region, the metal-insulator and antiferromagnetic transition occur simultaneously. To confirm the metal-insulator transition, momentum distribution functions $n(\vec{k})$ around the energy level crossing points are shown in Fig. 9, where the shape of $n(\vec{k})$ is qualitatively different between the metal and the insulator.

APPENDIX E: ABSENCE OF SINGULARITY IN ENERGY AS FUNCTION OF CONTROL PARAMETER

Figure 10 shows that the energy as functions of n (a) and U (b) look nonsingular around the MQCP at $U = 1.83$ and $t_{\perp} = 0.38$.

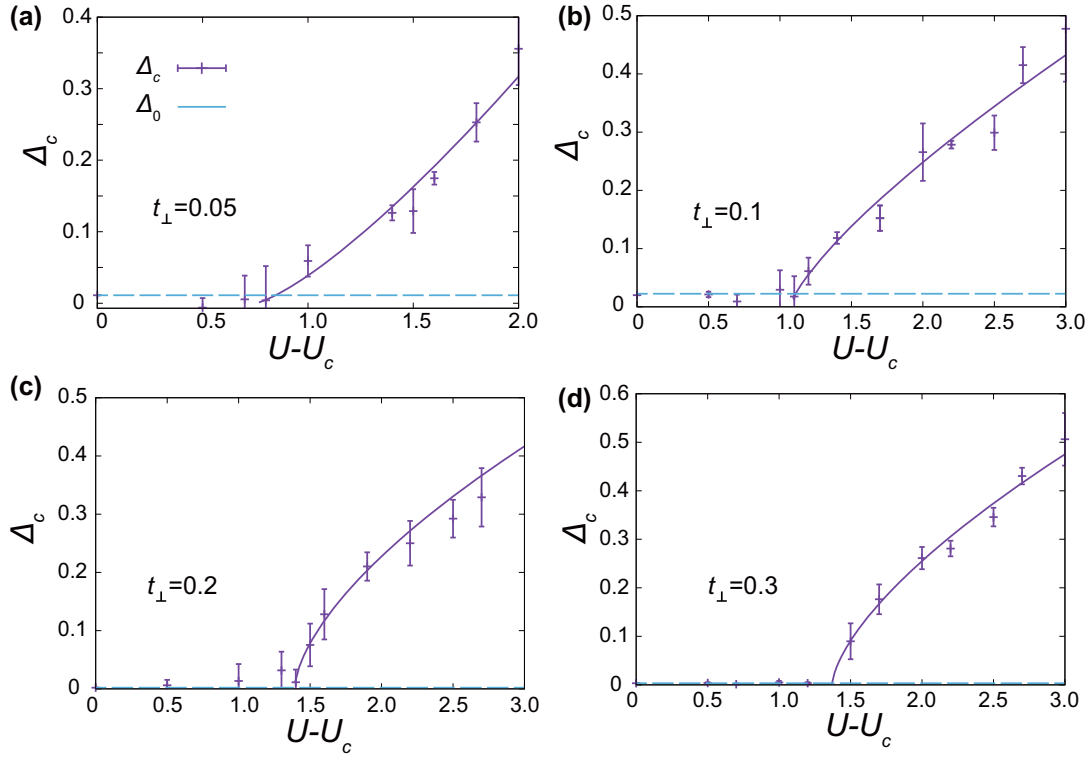


FIG. 7. Examples of charge gaps Δ_c for 28×28 sites in the cases of $t_{\perp} = 0.05$ (a), 0.1 (b), 0.2 (c) and 0.3 (d). Thin dashed blue lines are the finite-size gaps in the noninteracting case.

APPENDIX F: DETERMINATION OF ANTIFERROMAGNETIC TRANSITION AND ITS CRITICALITY

The universality of the magnetic transition may belong to a class different from the Mott transition. As well as metal-insulator transitions, we see the clear jumps of the staggered

magnetization m_s in the region of first-order transitions. However, the border between paramagnetic and antiferromagnetic phases is not straightforward in the region of continuous transitions. Here we first describe how U^{AF} is estimated and then the estimate of the critical exponent at the MQCP later.

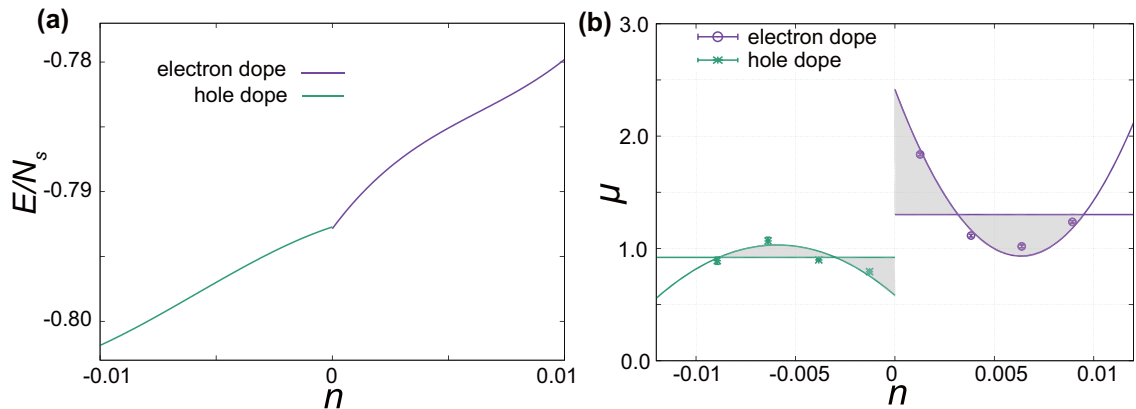


FIG. 8. An example of charge gap estimate by Maxwell rule. (a) Ground-state energy as a function of carrier density n at $t_{\perp} = t_{\perp}^{\text{MQCP}} = 0.38$ and $U = 2.5$ for 28×28 -site system. (b) Chemical potential μ vs n for the same case as panel (a). The Horizontal solid lines in both electron- and hole-doped regions represent the lines used for the Maxwell's construction, where the horizontal line is drawn to make the areas of the two shaded regions surrounded by the line and the curve equal. For the curve and line adjacent to $n = 0$, we count the area of the shaded domain surrounded by the curve, the horizontal line and the $n = 0$ vertical line. Then the two crossing points of the line and the curve determines the two points of the phase separation for each electron and hole side as assured by the thermodynamic stability. The difference in μ between electron and hole doped sides (the difference of μ between the two horizontal lines) gives the charge gap.

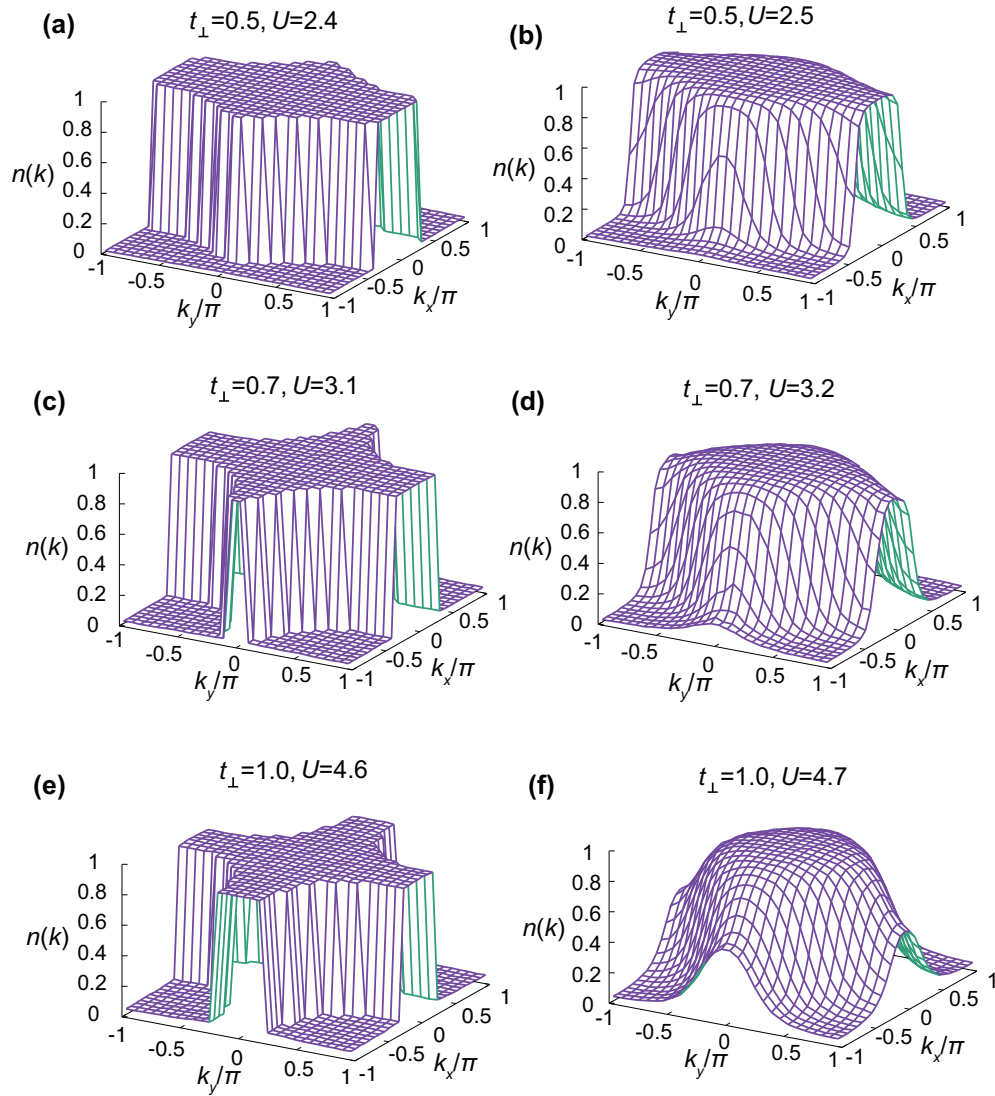


FIG. 9. Momentum distribution functions $n(\vec{k})$ for $t_\perp = 0.5, 0.7$ and 1.0 around the metal-insulator transition points. Panels (a), (c), (e) indicate the metallic phase with sharp Fermi surface, while panels (b), (d), (f) indicate the insulating phase without the Fermi surface.

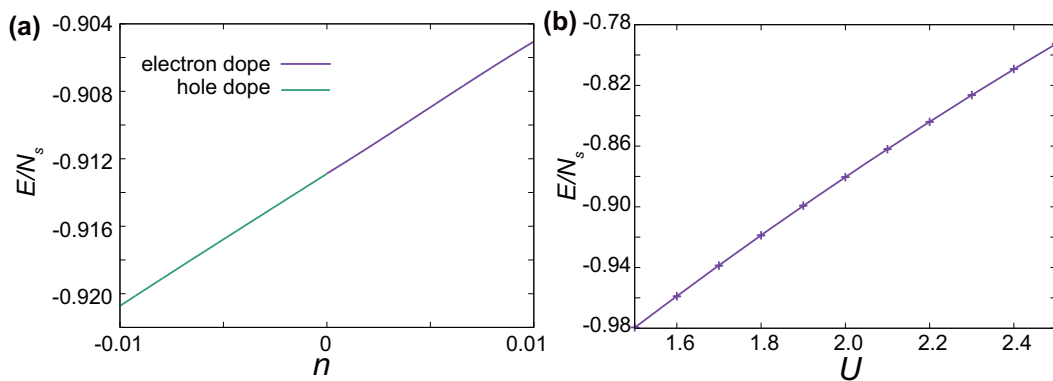


FIG. 10. Ground-state energy as a function of carrier density n (a) and U (b), which support the absence of the singular behavior.

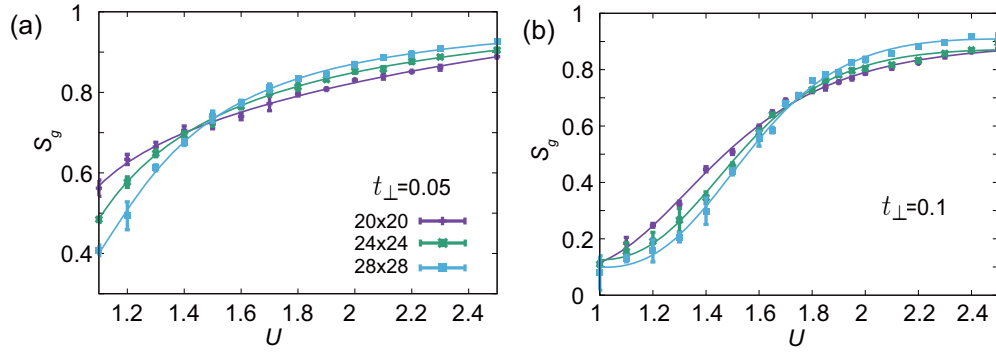


FIG. 11. Correlation-ratio plot for 20×20 , 24×24 , and 28×28 sites in the cases of (a) $t_{\perp} = 0.05$ and (b) $t_{\perp} = 0.1$. The crossing points suggest $U^{\text{AF}} \sim 1.48$ and 1.73 , respectively.

1. Antiferromagnetic transition determined by correlation ratio method

We determine the boundary of the antiferromagnetic phase by using the correlation-ratio method [35], where the correlation-ratio parameter S_g obtained from the spin structure factor $S(q)$ is given by

$$S_g \equiv 1 - \frac{S(\pi, \pi + \Delta q_y)}{S(\pi, \pi)}. \quad (\text{F1})$$

Here, $\pi + \Delta q_y$ is the nearest-neighbor \vec{k} -point to (π, π) . We plotted this ratio for 20×20 , 24×24 , and 28×28 sites, to determine the border of paramagnetic and antiferromagnetic phases. In the nonmagnetic region, S_g converges to zero with increasing system size, because $S(\vec{q})$ is finite and continuous in the thermodynamic limit. However, in the AF region, S_g converges to one by increasing the system size. It is empirically observed that the different-size curves cross and the crossing point does not sensitively depend on the system sizes, which serves as a good estimate of the transition point in thermodynamic limit [35,36]. We plot the curves and their crossing points for 20×20 , 24×24 , and 28×28 sites.

In the same way as fittings of energy and double occupancy, we interpolate the correlation-ratio parameter S_g as a function of U by assuming the rational function as

$$g(U) = \frac{a_0 U^2 + a_1 U + a_2}{a_3 U^2 + a_4 U + a_5}. \quad (\text{F2})$$

From this fitting we are able to estimate the correlation-ratio crossing point by the interpolation. The phase boundary of the magnetic transition in Fig. 1 is thus determined from the crossing points of S_g for 20×20 , 24×24 , and 28×28 sites. We show the correlation-ratio plot for 20×20 , 24×24 , and 28×28 sites in the cases of $t_{\perp} = 0.05$ and 0.1 in Fig. 11, where the metal-insulator transition is clearly different and the quantum spin liquid phase (NMI) is found. For $t_{\perp} = t_{\perp}^{\text{MQCP}} = 0.38$ the plot is shown in Fig. 12. Then the magnetic transition point is consistently estimated as $U^{\text{AF}} \sim 1.85 \pm 0.02$, which is close to $U^{\text{MQCP}} \sim 1.83 \pm 0.03$, but seems to be slightly larger within the error bar.

2. Critical exponent at antiferromagnetic transition

We here estimate the critical exponents for the antiferromagnetic transition at the MQCP. For this purpose, we adopt the finite-size scaling relation for the spin structure factor $S(q)$,

$$S(\pi, \pi) = L^{-z+2-\eta} f_m(uL^{1/\nu}), \quad (\text{F3})$$

where $u = (U - U^{\text{AF}})/U^{\text{AF}}$ and z represents the dynamical exponent while f_m is a scaling function and η is the exponent associated with the anomalous dimension.

As shown in Fig. 13, we obtain the exponent as

$$\nu = 0.52 \pm 0.02, \quad \text{and} \quad \eta + z = 1.9 \pm 0.1 \quad (\text{F4})$$

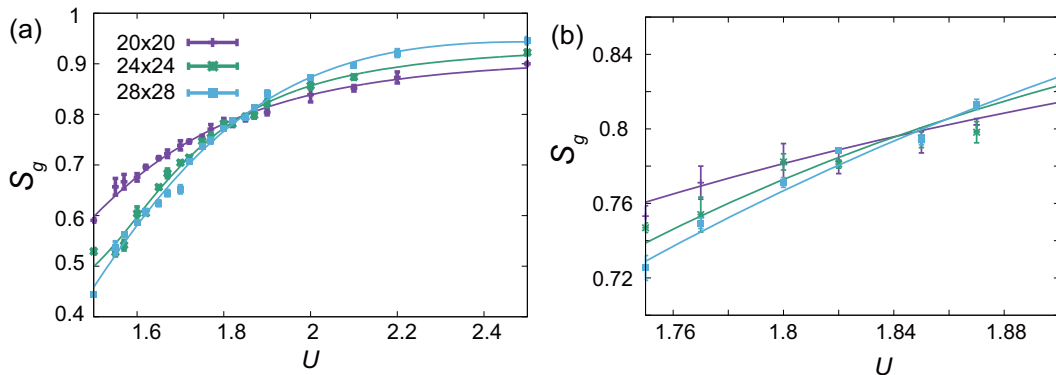


FIG. 12. Determination of the antiferromagnetic transition along $t_{\perp} = t_{\perp}^{\text{MQCP}} = 0.38$. Analysis by correlation-ratio method by using 20×20 , 24×24 , and 28×28 lattices is shown in wide region in panel (a) and the zoom-in plot in panel (b).

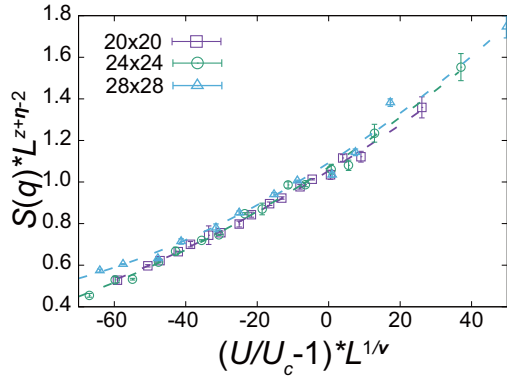


FIG. 13. Finite-size scaling of $S(\pi, \pi)$ by using scaling relation (F3). The data collapse to a single scaling curve is found for $\nu = 0.52 \pm 0.02$, and $\eta + z = 1.9 \pm 0.1$ with $U^{\text{AF}} = 1.85 \pm 0.02$.

if the scaling form (F3) is used with $U^{\text{AF}} = 1.85$ at $t_{\perp} = 0.38$. Moreover, if we assume the hyperscaling relation

$$\frac{\beta}{\nu} = \frac{z + d - 2 + \eta}{2}, \quad (\text{F5})$$

then we can estimate the critical exponent $\beta_{\text{AF}} = 0.49 \pm 0.03$, which turns out to be consistent with that of the mean-field theory ($\beta = 0.5$). This is justified when $z \sim 2$ so that $d + z = 4$ assures that the present system is located just at the upper critical dimension in the conventional framework of Ising or Hertz-Moriya [37,38] and the critical exponents are marginally given by the mean-field values for the symmetry breaking transition. This is also consistent with $z + \eta \sim 2$ resulting in $\eta \sim 0$, indicating the absence of the anomalous dimension. Then $\gamma = 1$ and $\delta = 3$ derived from the scaling relation indicate divergent fluctuations in contrast with the universality of the metal-insulator transition. A large $z(\sim 2)$ instead of the normal value $z = 1$ expected for the antiferromagnetic spin wave dispersion could be the consequence of the proximity from the MQCP. Instead, it is conceivable that nonnegligible $\eta > 0$ makes $d + z < 4$ so that the deviation from the mean-field value exists, which may drive z to decrease from 2, though the presence of the diverging fluctuations characterized by $\gamma > 1$ and $\delta > 1$ would not change. These issues should be carefully examined in the future in the region close to the transition point if U^{AF} is different from U^{MQCP} . Of course, the AF long-range order requires the multidimensionality $d \geq 2$ of the system. Although the background broad peak reflects the moderate anisotropy of the Hamiltonian, the spin structure factor $S(q)$ shown in Fig. 14 clearly demonstrates that the spin correlation is 2D isotropic behavior for a critical sharp peak at (π, π) even at MQCP.

APPENDIX G: DOUBLE OCCUPANCY CORRELATION

Spatial correlation of double occupancy D is defined in Eq. (12). The spatial correlation of the fluctuation of D defined by Eq. (26) is plotted in Fig. 15, where the fitting of $Q(\vec{r})$ suggests $z + \eta = 3.3 \pm 0.8$ from Eq. (27). The value is consistent with the present scaling theory that requires $z + \eta = 4$.

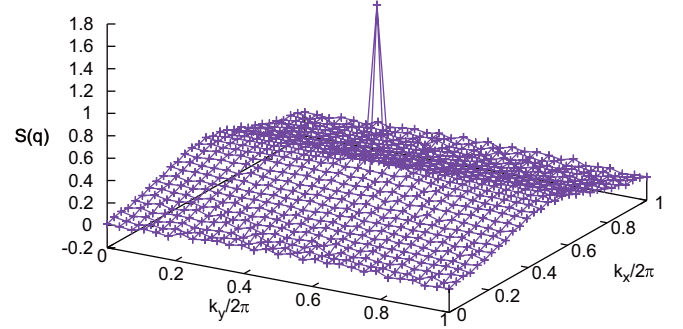


FIG. 14. Spin structure factor at MQCP.

APPENDIX H: SIZE EXTRAPOLATION OF DOUBLE OCCUPANCY

To analyze the criticality by using the double occupancy, we perform the size extrapolations of D by using the following formulas:

$$D(L) = D_{\infty} + \begin{cases} b_M/L^2 & (\text{metal}) \\ b_I/L & (\text{insulator}) \end{cases}, \quad (\text{H1})$$

where D_{∞} is the double occupancy at the thermodynamic limit and b_M (b_I) is the fitting parameter in the metallic (insulating) phase. Examples of the fitting are shown in Fig. 16. The error bars in Fig. 2 of the main article are determined by the square root of the mean square error of the fitting.

APPENDIX I: DECOUPLING OF METAL-INSULATOR AND ANTIFERROMAGNETIC TRANSITIONS

The metal-insulator transition (MIT) is often intertwined with magnetic fluctuations. A phenomenology that will capture both the MIT and the spin degrees of freedom necessitates a scalar order parameter $\Phi(\mathbf{x}, \tau)$ that captures the doublon occupancy, as well as a normalized vector order parameter $\mathbf{n}(\mathbf{x}, \tau)$ that captures the antiferromagnetic fluctuations. The field theory has to possess a $Z_2 \times O(3)$ global symmetry, $\Phi(\mathbf{x}, \tau) \rightarrow -\Phi(\mathbf{x}, \tau)$ and $\mathbf{n}(\mathbf{x}, \tau) \rightarrow O\mathbf{n}(\mathbf{x}, \tau)$ with O an

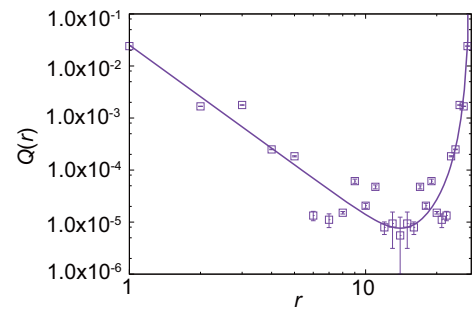


FIG. 15. Spatial correlation of double-occupancy fluctuation in x direction defined in Eq. (26). Error bars are those of statistical errors in the Monte Carlo sampling. The fitting curve is obtained by using the form $Q(\vec{r}) \propto 1/|r|^{z+\eta} + \sum_{n \neq (0,0)} [(1/|r + L\vec{n}|^{z+\eta}) - (1/|L\vec{n}|^{z+\eta})]$ to fit the data at $r \geq 3$ to estimate the asymptotic form at long distance. It suggests more or less isotropic power-law decay with $z + \eta = 3.3 \pm 0.8$ by taking account of the combined errors of the fitting and the Monte Carlo sampling.

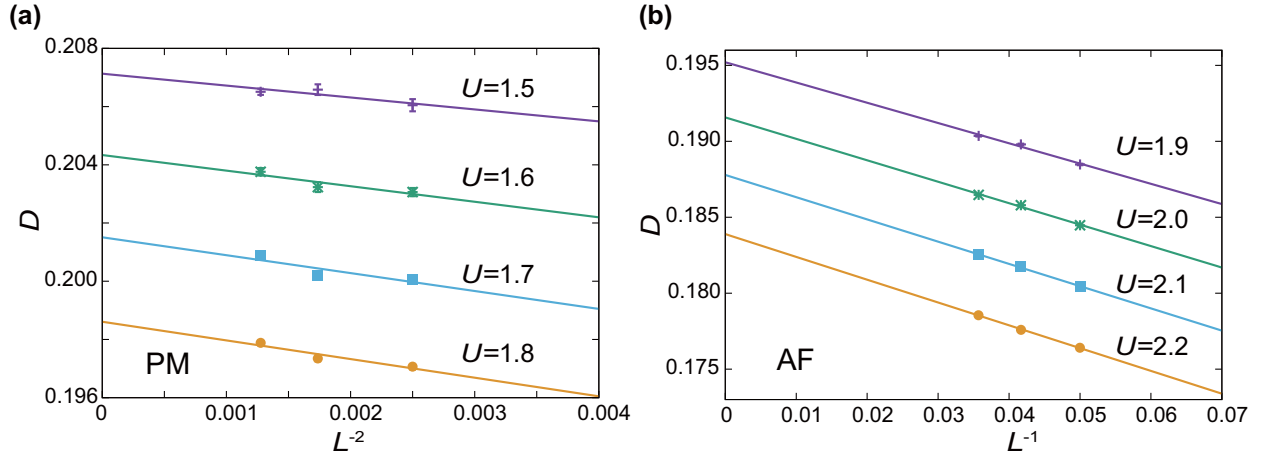


FIG. 16. Size extrapolation of the double occupancy at $t_{\perp}^{\text{MQCP}} = 0.38$ by using Eq. (H1). The VMC data of the double occupancy are plotted for the metallic phase ($U = 1.5, 1.6, 1.7$, and 1.8) (a) and for the insulating phase ($U = 1.9, 2.0, 2.1$, and 2.2) (b) by using the lattices with $L = 20, 24$, and 28 .

orthogonal matrix, and effective Lagrangian reads

$$L = L_{\Phi} + L_n + L_{\text{int}}. \quad (11)$$

It accounts for the dynamics of the scalar field and the vector field as well as the interaction between both of them. We will refrain from writing down explicit forms for L_{Φ} and L_n , since the only information we need to assess if L_{int} is relevant or not at criticality are the scaling dimensions of $\mathbf{n}(\mathbf{x}, \tau)$ and $\Phi(\mathbf{x}, \tau)$. Assuming a singular spatiotemporal length scale λ , and for a given dynamical exponent z , we expect that the correlation function of the order parameter Φ at criticality follows

$$\langle \Phi(\lambda \mathbf{x}, \lambda^z \tau) \Phi(\lambda \mathbf{x}', \lambda^z \tau') \rangle \propto \frac{1}{\lambda^{2\Delta_{\Phi}}} \langle \Phi(\mathbf{x}, \tau) \Phi(\mathbf{x}', \tau') \rangle, \quad (12)$$

where Δ_{Φ} is represented by the exponents of the MQCP as $2\Delta_{\Phi} = d + z + \eta - 2$. For those who are not familiar with this critical scaling exponent Δ_{Φ} , see below an example of the simple ϕ^4 model. At the MQCP our estimates are $z \sim 2$ and $\eta \sim 2$ and the equal time doublon-doublon correlation functions are consistent with $\Delta_{\Phi} \simeq 2$. A similar form holds for the $O(3)$ order parameter \mathbf{n} . We are now in a position to perturbatively understand if the coupling between the spin and doublon degrees of freedom is irrelevant, marginal or relevant. The most relevant symmetry allowed interaction between the $O(3)$ and Z_2 fields reads

$$L_{\text{int}} = g \int d^2 \mathbf{x} d\tau \Phi(\mathbf{x}, \tau)^2 (\nabla_{\mathbf{x}} \mathbf{n}(\mathbf{x}, \tau))^2 + \dots \quad (13)$$

We note that due to the normalization of the $O(3)$ order parameter $\Phi^2 \mathbf{n}^2$ does not provide a spin-charge coupling. The ellipsis denotes higher order terms under a scale transformation. Under a scale transformation, the interaction terms transforms as

$$g \rightarrow g \lambda^{z-2\Delta_{\Phi}-2\Delta_n}. \quad (14)$$

As mentioned above, we know that for the MQCP $\Delta_{\Phi} \simeq 2$ and that $z \simeq 2$. As a result, and for any $\Delta_n > 0$, g scales to zero under successive coarse graining scale transformations. The above provides a compelling argument supporting the

notion that the charge and spin transitions are, in the RG sense, independent of each other at the MQCP.

Here, we supplement the relation of the scaling exponent of the correlation defined in Eq. (12) to the general framework of the scaling theory in a simple example of conventional ϕ^4 theory for the readers who are not familiar with the scaling theory of quantum systems. The nondimensional ϕ^4 Hamiltonian H_{ϕ} is given by

$$H[\phi] = \int d^d r \left[\frac{1}{2} (\nabla \phi)^2 + \frac{A}{2} \phi^2 + \frac{B}{4} \phi^4 \right], \quad (15)$$

with coefficients A and B . From the assumption of a single length scale λ , this classical ϕ^4 Hamiltonian requires the scaling of ϕ from the first term as

$$[\phi] = \lambda^{1-\frac{d+\eta}{2}}, \quad (16)$$

where η is the anomalous dimension to account for the relation of λ and the diverging correlation length ξ . From the second and third terms, we obtain similarly $[A] = \lambda^{-2}$ and $[B] = \lambda^{d+\eta-4}$, respectively. When quantum dynamics is in-

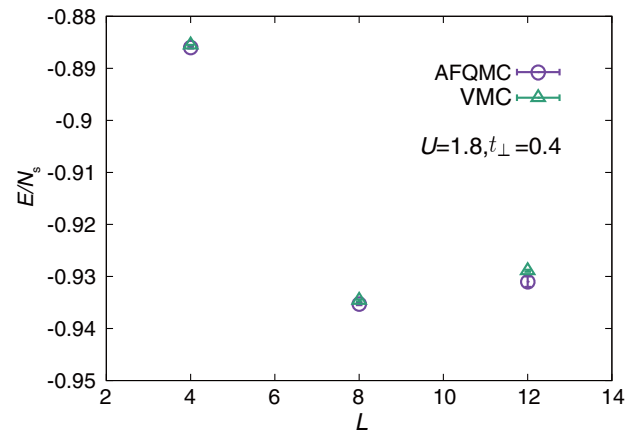


FIG. 17. Comparison of ground-state energy between the VMC and AFQMC for $L = 4, 8$, and 12 at $t = 1$, $U = 1.8$, and $t_{\perp} = 0.4$, which is close to the MQCP.

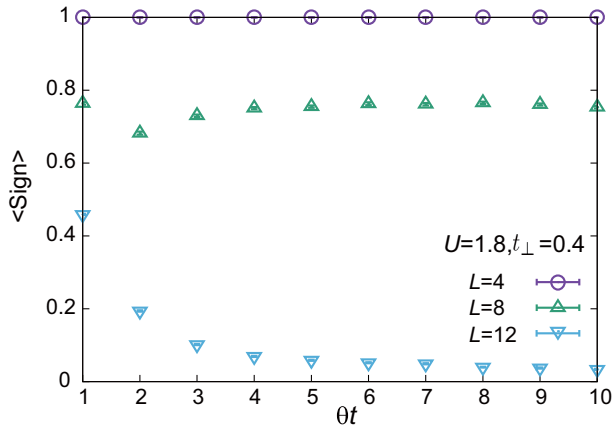


FIG. 18. Averaged sign in AFQMC as a function of the effective imaginary time θt at the same parameter as Fig. 17.

roduced, a mapping of a d -dimensional quantum system to $d+z$ -dimensional classical representation tells us that we need to replace d with $d+z$. Here, z is the dynamical exponent to represent the scaling of timescale $[\tau] = [\lambda]^z$. From this we obtain the criticality of correlation function from the scaling of ϕ [Eq. (16)] as

$$\langle \phi(\lambda \mathbf{x}, \lambda^z \tau) \phi(\lambda \mathbf{x}', \lambda^z \tau') \rangle \propto \frac{1}{\lambda^{2\Delta_\phi}} \langle \phi(\mathbf{x}, \tau) \phi(\mathbf{x}', \tau') \rangle, \quad (17)$$

with $2\Delta_\phi = d + z + \eta - 2$.

TABLE I. Comparison of the ground-state energy for the same parameter as Fig. 17 calculated by the present VMC and AFQMC. The average sign of the AFQMC simulations, $\langle \text{sign} \rangle$ at the effective inverse temperature $\theta t = 10$, is also shown.

VMC	E/N_s	
$L = 4$	-0.88554 ± 0.00004	
$L = 8$	-0.9346 ± 0.0002	
$L = 12$	-0.9289 ± 0.0002	
AFQMC	E/N_s	$\langle \text{sign} \rangle$
$L = 4$	-0.8860 ± 0.0002	1.0000 ± 0.0001
$L = 8$	-0.9353 ± 0.0002	0.754 ± 0.003
$L = 12$	-0.931 ± 0.001	0.034 ± 0.001

APPENDIX J: ADDITIONAL BENCHMARK DATA

Here we show the benchmark in comparison to the auxiliary-field quantum Monte Carlo (AFQMC) calculation [39–41]. Figure 17 shows the energy comparison of the present model near the MQCP, namely at $U/t = 1.8$ and $t_{\perp} = 0.4$ up to $L = 12$, between the present VMC and the AFQMC calculation which should be exact within the statistical error after convergence to the ground state. The agreement of these two methods is satisfactory in these clusters. However, the average sign of the AFQMC rapidly approaches zero with increasing system size as is shown in Fig. 18. Beyond $L = 12$, it is hard to obtain meaningful results by AFQMC. The estimated ground-state energies and the averaged sign are also listed in Table I. The AFQMC calculations were carried out with the ALF-library [42].

- [1] M. Imada, A. Fujimori, and Y. Tokura, Metal-insulator transitions, *Rev. Mod. Phys.* **70**, 1039 (1998).
- [2] Y. Zhou, K. Kanoda, and T.-Kai Ng, Quantum spin liquid states, *Rev. Mod. Phys.* **89**, 025003 (2017).
- [3] R. Kato, Development of π -electron systems based on [M(dmit)2] (M = Ni and Pd; dmit: 1,3-dithiole-2-thione-4,5-dithiolate) anion radicals, *Bull. Chem. Soc. Jpn.* **87**, 355 (2014).
- [4] T. Misawa and M. Imada, Superconductivity and its mechanism in an *ab initio* model for electron-doped LaFeAsO, *Nat. Commun.* **5**, 5738 (2014).
- [5] M. Imada and T. J. Suzuki, Excitons and dark fermions as origins of Mott gap, pseudogap and superconductivity in cuprate superconductors—General concept and basic formalism based on gap physics, *J. Phys. Soc. Jpn.* **88**, 024701 (2019).
- [6] M. Imada, Charge order and superconductivity as competing brothers in cuprate high- T_c superconductors, *J. Phys. Soc. Jpn.* **90**, 111009 (2021).
- [7] M. Imada, Universality classes of metal-insulator transitions in strongly correlated electron systems and mechanism of high-temperature superconductivity, *Phys. Rev. B* **72**, 075113 (2005).
- [8] C. Castellani, C. Di Castro, D. Feinberg, and J. Ranninger, New Model Hamiltonian for the Metal-Insulator Transition, *Phys. Rev. Lett.* **43**, 1957 (1979).
- [9] P. Limelette, A. Georges, D. Jérôme, P. Wzietek, P. Metcalf, and J. M. Honig, Universality and critical behavior at the Mott transition, *Science* **302**, 89 (2003).
- [10] T. Misawa and M. Imada, Quantum criticality around metal-insulator transitions of strongly correlated electron systems, *Phys. Rev. B* **75**, 115121 (2007).
- [11] G. Kotliar, S. Murthy, and M. J. Rozenberg, Compressibility Divergence and the Finite Temperature Mott Transition, *Phys. Rev. Lett.* **89**, 046401 (2002).
- [12] D. Tahara and M. Imada, Variational Monte Carlo method combined with quantum-number projection and multi-variable optimization, *J. Phys. Soc. Jpn.* **77**, 114701 (2008).
- [13] T. Misawa and M. Imada, Origin of high- T_c superconductivity in doped Hubbard models and their extensions: Roles of uniform charge fluctuations, *Phys. Rev. B* **90**, 115137 (2014).
- [14] T. Misawa, S. Morita, K. Yoshimi, M. Kawamura, Y. Motoyama, K. Ido, T. Ohgoe, M. Imada, and T. Kato, mVMC—Open-source software for many-variable variational Monte Carlo method, *Comput. Phys. Commun.* **235**, 447 (2019).
- [15] H. Terletska, J. Vučičević, D. Tanasković, and V. Dobrosavljević, Quantum Critical Transport Near the Mott Transition, *Phys. Rev. Lett.* **107**, 026401 (2011).

- [16] T. Furukawa, K. Miyagawa, H. Taniguchi, R. Kato, and K. Kanoda, Quantum criticality of Mott transition in organic materials, *Nat. Phys.* **11**, 221 (2015).
- [17] F. H. L. Essler and A. M. Tsvelik, Weakly coupled one-dimensional Mott insulators, *Phys. Rev. B* **65**, 115117 (2002).
- [18] P. Ribeiro, P. D. Sacramento, and K. Penc, Finite-energy spectral function of an anisotropic two-dimensional system of coupled Hubbard chains, *Phys. Rev. B* **84**, 045112 (2011).
- [19] B. Lenz, S. R. Manmana, T. Pruschke, F. F. Assaad, and M. Raczkowski, Mott Quantum Criticality in the Anisotropic 2D Hubbard Model, *Phys. Rev. Lett.* **116**, 086403 (2016).
- [20] M. Raczkowski, F. F. Assaad, and M. Imada, Local moments versus itinerant antiferromagnetism: Magnetic phase diagram and spectral properties of the anisotropic square lattice Hubbard model, *Phys. Rev. B* **103**, 125137 (2021).
- [21] J. Vučković, H. Terletska, D. Tanasković, and V. Dobrosavljević, Finite-temperature crossover and the quantum Widom line near the Mott transition, *Phys. Rev. B* **88**, 075143 (2013).
- [22] B. H. Moon, Metal-insulator transition in two-dimensional transition metal dichalcogenides, *Emergent Mater.* **4**, 989 (2021).
- [23] T. Li, S. Jiang, L. Li, Y. Zhang, K. Kang, J. Zhu, K. Watanabe *et al.*, Continuous Mott transition in semiconductor moire superlattices, *Nature (London)* **597**, 350 (2021).
- [24] H. Eisenlohr, S.-Sup B. Lee, and M. Vojta, Mott quantum criticality in the one-band Hubbard model: Dynamical mean-field theory, power-law spectra, and scaling, *Phys. Rev. B* **100**, 155152 (2019).
- [25] Y. Yamaji, T. Misawa, and M. Imada, Quantum and topological criticalities of Lifshitz transition in two-dimensional correlated electron systems, *J. Phys. Soc. Jpn.* **75**, 094719 (2006).
- [26] K. Ido, T. Ohgoe, and M. Imada, Competition among various charge-inhomogeneous states and d -wave superconducting state in Hubbard models on square lattices, *Phys. Rev. B* **97**, 045138 (2018).
- [27] A. S. Darmawan, Y. Nomura, Y. Yamaji, and M. Imada, Stripe and superconducting order competing in the Hubbard model on a square lattice studied by a combined variational Monte Carlo and tensor network method, *Phys. Rev. B* **98**, 205132 (2018).
- [28] S. Sorella, Generalized Lanczos algorithm for variational quantum Monte Carlo, *Phys. Rev. B* **64**, 024512 (2001).
- [29] K. Takai, K. Ido, T. Misawa, Y. Yamaji, and M. Imada, Finite-temperature variational Monte Carlo method for strongly correlated electron systems, *J. Phys. Soc. Jpn.* **85**, 034601 (2016).
- [30] M. C. Gutzwiller, Effect of Correlation on the Ferromagnetism of Transition Metals, *Phys. Rev. Lett.* **10**, 159 (1963).
- [31] R. Jastrow, Many-body problem with strong forces, *Phys. Rev.* **98**, 1479 (1955).
- [32] L. F. Tocchio, F. Becca, and S. Sorella, Hidden Mott transition and large- u superconductivity in the two-dimensional Hubbard model, *Phys. Rev. B* **94**, 195126 (2016).
- [33] Y. Nomura and M. Imada, Dirac-Type Nodal Spin Liquid Revealed by Refined Quantum Many-Body Solver Using Neural-Network Wave Function, Correlation Ratio, and Level Spectroscopy, *Phys. Rev. X* **11**, 031034 (2021).
- [34] K. Ido, K. Yoshimi, T. Misawa, and M. Imada, Unconventional dual 1D-2D quantum spin liquid revealed by ab initio studies on organic solids family, *npj Quantum Mater.* **7**, 48 (2022).
- [35] R. K. Kaul, Spin Nematics, Valence-Bond Solids, and Spin Liquids in SO(n) Quantum Spin Models on the Triangular Lattice, *Phys. Rev. Lett.* **115**, 157202 (2015).
- [36] S. Pujari, T. C. Lang, G. Murthy, and R. K. Kaul, Interaction-Induced Dirac Fermions from Quadratic Band Touching in Bilayer Graphene, *Phys. Rev. Lett.* **117**, 086404 (2016).
- [37] J. A. Hertz, Quantum critical phenomena, *Phys. Rev. B* **14**, 1165 (1976).
- [38] T. Moriya, *Spin Fluctuations in Itinerant Electron Magnetism*, Springer Series in Solid-State Sciences, No. 56 (Springer, Berlin, 1985).
- [39] S. Sorella, S. Baroni, R. Car, and M. Parrinello, A novel technique for the simulation of interacting fermion systems, *Europhys. Lett.* **8**, 663 (1989).
- [40] M. Imada and Y. Hatsugai, Numerical Studies on the Hubbard Model and the t - J Model in One- and Two-Dimensions, *J. Phys. Soc. Jpn.* **58**, 3752 (1989).
- [41] F. Assaad and H. Evertz, *World-line and Determinantal Quantum Monte Carlo Methods for Spins, Phonons, and Electrons*, in *Computational Many-particle Physics*, Springer Series in Solid-State Sciences, No. 56 (Springer, Berlin, 2008).
- [42] F. F. Assaad, M. Bercx, F. Goth, A. Götz, J. S. Hofmann, E. Huffman, Z. Liu, F. Parisen Toldin, J. S. E. Portela, and J. Schwab, The ALF (Algorithms for Lattice Fermions) project release 2.0. Documentation for the auxiliary-field quantum Monte Carlo code, *SciPost Phys. Codebases* **1** (2022).